

Real-time holographic lensless micro-endoscopy through flexible fibers via Fiber Bundle Distal Holography (FiDHo)

Noam Badt

Hebrew University of Jerusalem

Ori Katz (✉ orik@mail.huji.ac.il)

Hebrew University of Jerusalem

Article

Keywords: Fiber-based micro-endoscopes, tissue imaging, Fiber Bundle Distal Holography (FiDHo)

Posted Date: June 23rd, 2021

DOI: <https://doi.org/10.21203/rs.3.rs-528386/v1>

License:  This work is licensed under a Creative Commons Attribution 4.0 International License.

[Read Full License](#)

Version of Record: A version of this preprint was published at Nature Communications on October 13th, 2022. See the published version at <https://doi.org/10.1038/s41467-022-33462-y>.

1 **Title**

2 Real-time holographic lensless micro-endoscopy
3 through flexible fibers via Fiber Bundle Distal Holography (FiDHo)

4 **Authors**

5 Noam Badt¹
6 Ori Katz^{1*}

7 **Affiliations**

8 ¹ Department of Applied Physics, Hebrew University of Jerusalem, Jerusalem 9190401,
9 Israel.
10 *orik@mail.huji.ac.il

11 **Abstract**

12 Fiber-based micro-endoscopes are a critically important tool for minimally-invasive
13 deep-tissue imaging. However, the state-of-the-art micro-endoscopes cannot perform three-
14 dimensional imaging through dynamically-bent fibers without the use of bulky optical
15 elements such as lenses and scanners at the distal end, increasing the footprint and tissue-
16 damage. Great efforts have been invested in developing approaches that avoid distal bulky
17 optical elements. However, the fundamental barrier of dynamic optical wavefront-
18 distortions in propagation through flexible fibers, limits current approaches to nearly-static
19 or non-flexible fibers. Here, we present an approach that allows holographic 3D bend-
20 insensitive, coherence-gated, micro-endoscopic imaging, using commercially available
21 multi-core fibers (MCFs). We achieve this by adding a miniature partially-reflecting mirror
22 to the distal fiber-tip, allowing to perform low-coherence full-field phase-shifting
23 holography. We demonstrate widefield diffraction-limited reflection imaging of amplitude
24 and phase targets through dynamically bent fibers at video-rates. Our approach holds
25 potential for label-free investigations of dynamic samples.
26

MAIN TEXT

Introduction

Flexible optical micro-endoscopes are an important tool for a wide variety of applications, from clinical procedures to biomedical investigations, where micron-scale structures such as single neurons are imaged [1, 2] or optically excited [3] at depths beyond the reach of conventional microscopes. Developing a flexible, 3D, video-rate, label-free micro-endoscope with a minimal footprint is thus a sought-after goal for minimally invasive deep-tissue imaging.

In the quest for this goal various micro-endoscopes have been developed in recent years. One set of solutions consists of micro-endoscopes that are based on single-mode fibers. While bend-insensitive, these require distal optical elements such as scanners and lenses [1], or spectral dispersers [4, 5] to produce an image. Such distal elements significantly enlarge the endoscope diameter, increasing tissue damage, and consequently limiting its use for minimally-invasive deep-tissue imaging.

Another set of solutions utilize imaging fiber bundles, also known as multi-core fibers (MCFs). These consist of thousands of cores closely packed together. Conventionally, each core functions as a single pixel, either by direct contact with the target or by the addition of a GRIN lens at the distal end [1, 2]. While straightforward to use, conventional bundle-based endoscopes suffer from limited resolution, pixelation and a small and fixed working distance with poor axial sectioning capability. Even though axial-sectioning can be improved by using temporal coherence-gating [6, 7] or confocal or other structured illumination [8], many of the inherent limitations remain. These include pixelation artefacts, limited resolution, and a fixed working distance. Moreover, strong spurious reflections from the fiber tips limit the applicability of such approaches for label-free imaging.

An emerging set of approaches for lensless endoscopes that go beyond many of the conventional limitations are based on the measurement of the fiber transmission-matrix (TM), with or without an additional distal mask or diffuser. This allows compensation of the complex coherent or incoherent transfer-function of these multi-mode systems, either digitally [10, 11, 12, 13, 14, 15, 16] or via wavefront-shaping [17, 18, 19, 20, 21, 22, 23, 24]. However, solutions that are based on a single TM measurement without the addition of a distal element is limited to non-flexible fibers, since fiber bending strongly distorts the TM. The TM may be estimated using a large number of measurements and complex computation, but do not allow video-rate imaging or imaging through dynamically bent fibers [25, 26, 27]. Alternative, speckle based incoherent imaging approaches [11, 12, 13, 14], suffer from very low contrast of the acquired images. MCFs with bend-insensitive inter-core phase relations have been fabricated [28]. However, these rely on a relatively small number of single-mode cores, suffering from low collection-efficiency and fill-factor.

Related to the TM-based approaches, Czarske et al. [29, 30, 31] have demonstrated in-situ measurement of the fiber phase-distortions by adding a partially-reflecting mirror to the MCF distal-facet, and correction using a spatial light modulator (SLM). However, as imaging is performed by raster scanning a phase-corrected focus, correction of dynamic distortions is challenging, and fluorescence labeling is required.

Label-free holographic approaches to endoscopy that utilize MCFs as intensity-only image-guides have been put forward over the years [32, 33, 34]. However, these rely on additional fibers for illumination, suffer from poor axial-sectioning, and limited field of view (FoV) or coherent background due to twin image artefacts.

Here we present a simple approach that allows holographic 3D, calibration-free, bend-insensitive, coherence-gated, micro-endoscopic imaging utilizing commercially available MCFs. We achieve this by adding a miniature partially reflecting mirror to the distal fiber-tip (Fig. 1), which allows us to perform low-coherence full-field phase-shifting

77 holography at video-rate, with diffraction-limited resolution, where the coherent
 78 illumination is provided through a single MCF core.

81 Results

82 Principle

83 The optical setup for realizing our approach is schematically depicted in Fig. 1. It is
 84 based on the excitation of a single MCF core by two delayed replicas of a low coherence
 85 illuminating beam (Fig. 1A). The two beams co-propagate in the same core along the MCF.
 86 At the MCF distal end, the reflection of the first arriving beam from the target interferes
 87 with the reflection of the second ("reference") beam from the distal partially reflecting
 88 mirror (Fig. 1B). The interference intensity pattern is collected by the MCF cores (Fig. 1C)
 89 and relayed back to the proximal end where it is imaged on a camera (Fig. 1A).

90 The object complex field at the distal facet is reconstructed from $N \geq 3$ camera
 91 images via low-coherence phase-shifting holography, which is performed by controlling the
 92 phase of the reference beam (Fig. 1A). The use of a low-coherence source allows effective
 93 rejection of all spurious reflections by setting the time delay between the two excitation
 94 beams, τ , to match the object distance from the mirror, z_0 : $\tau = 2z_0/c$. Both the time
 95 delay, τ , and the phase-shifting are performed using the same interferometer that produces
 96 the two excitation beams.

97 The recorded hologram at the n -th phase shift, I_n , is the interference pattern from
 98 the diffracted object field, E_o , and the known, fixed spherical reference field, E_r , that is
 99 reflected from the distal mirror: $I_n(x, y) = |E_o(x, y) + E_r(x, y)e^{i\varphi_n}|^2$, where $\varphi_n = \frac{n}{N}2\pi$ is
 100 the phase added to the reference field. Importantly, the recorded interference intensity
 101 pattern is insensitive to fiber bending since the MCF faithfully relays the intensity images.
 102 Finally, the 3D object field is digitally reconstructed from the recorded field at the distal
 103 facet via back-propagation, as explained below.

104 Reconstruction process

105 The reflected object field at the fiber distal tip, E_o , is reconstructed from $N \geq 3$
 106 camera frames, I_n (Fig. 2A), by phase-shifting interferometry, followed by normalization
 107 with the conjugate of the known reference field, E_r^* (Fig. 2B):

$$108 \quad E_o(x, y) = \frac{1}{E_r^*(x, y)} \sum_{n=1}^N I_n(x, y) e^{i\varphi_n} \quad (1)$$

109 where E_r^* is approximated as a Gaussian beam from the theoretical first mode of a
 110 single fiber core.

111 3D reconstruction is then performed by back-propagation of the recorded field (Fig.
 112 2D), E_o , to any desired distance from the fiber facet, z_{prop} , and normalization by the
 113 expected illumination field amplitude and phase $E_{illum}(x, y, z_{prop})$:

$$114 \quad O(x, y, z_{prop}) = \frac{\mathcal{P}_{-z_{prop}}(E_o(x, y))}{E_{illum}(x, y, z_{prop})} \quad (2)$$

115 Where O is the reconstructed object complex reflection coefficient, $\mathcal{P}_{-z_{prop}}$ is the
 116 angular spectrum propagation operator by a distance $-z_{prop}$, and E_{illum} is approximated as
 117 a Gaussian beam from the theoretical first mode of a single fiber core. A digitally refocused
 118 sharp image of the object amplitude and phase is obtained (Fig. 2D) at the propagation
 119 distance $z_{prop} = z_0 + z_m$, where z_0 is the object-mirror distance and z_m is the mirror-fiber
 120 distance (Fig. 1B). The object distance can also be found from the low coherence holograms

121 by scanning the time delay, τ , and plotting the total energy of the reconstructed field at each
122 time delay (Fig. 2C).

123 As can be observed in (Fig. 3A-H), unlike conventional MCF-based endoscopes, the
124 holographic reconstruction is un-pixelated, since the MCF pixelation occurs at a difference
125 axial plane. The MCF pixelation at the fiber facet, which may introduce ghosting, is
126 removed using simple interpolation (see “Digital filtering of MCF pixelation” section).

127 Beyond the 3D holographic amplitude and phase label-free reconstruction, FiDHo
128 has several additional merits: it is insensitive to dynamic random phase distortions
129 introduced by fiber bending, the full-field reconstruction requires only 3 frames, allowing
130 video-rate imaging, and the low-coherence gating improves axial sectioning. In the next
131 sections we experimentally demonstrate each of these merits.

132 **Resolution and field-of-view**

133 To evaluate the system resolution and FoV, we performed several sets of
134 experiments using reflective targets placed at different distances from the fiber (Fig. 3).
135 Unlike conventional MCF-based microendoscopy, where each fiber core serves as one
136 imaging pixel and the resolution is limited by the core-to-core pitch (Fig. 3A), in FiDHo the
137 resolution is diffraction-limited and the images are unpixelated (Fig. 3C-D). Specifically,
138 FiDHo easily resolves group 7 element 4 of a USAF resolution target, signifying resolution
139 better than $2.7\mu\text{m}$ (Fig. 3G). More than two folds improvement over conventional contact
140 mode (Fig. 3E). In addition to imaging a USAF resolution target at several distances (Fig.
141 3C,D), a precise quantification of the resolution and FoV were performed by imaging a
142 knife-edge mirror and a large mirror respectively (Fig. 3I, J). Interestingly, and as expected
143 from the theoretical analysis (see section S1), the resolution and FoV are independent of
144 imaging distance for distances of $z_{obj} < D_{fiber}/2NA - z_m$, where D_{fiber} is the MCF
145 diameter. The resolution is diffraction limited to the fiber bundle numerical aperture (NA),
146 and the FoV is half the fiber diameter. For our experimental parameters ($z_m \approx 2\text{mm}$,
147 $D_{fiber} \approx 600\mu\text{m}$), the measured resolution and FoV ($300\mu\text{m}$, width) indicate an effective
148 NA of $NA_{eff} \sim 0.15$, which is in line with the fiber parameters (Schott 153385) and the
149 interpolation performed (see “Digital filtering MCF pixelation“ section).

150 **Phase-contrast imaging**

151 The holographic nature of FiDHo has inherently phase-contrast imaging capability,
152 important for the study of a wide variety of biological targets that presents very low
153 reflection or absorption contrast and is not available in conventional endoscopes [35].

154 To demonstrate phase-contrast imaging, we imaged human cheek cells placed on a
155 glass slide immersed in water. While the cells are not visible in the reconstructed amplitude
156 (Fig. 4A), the reconstructed phase clearly reveals the cells (Fig. 4B), as is validated by a
157 transmission image of the sample recorded by a reference distal camera (Fig. 4C,D).

158 **Video-rate and sensitivity to bending**

159 An important advantage of FiDHo is its high frame-rate. A single FiDHo frame
160 requires three camera frames, and thus is limited only by the camera framerate.
161 Supplementary Movie S1 demonstrates reconstruction of a moving target at 50 FPS.
162 Individual frames are shown in Fig. 5A.

163 An additional major advantage of FiDHo is its inherent low sensitivity to fiber
164 bending in both illumination and detection, an important requirement for *in-vivo* and freely-
165 behaving animal studies [3, 36]. In the illumination path, since both the illumination and
166 reference beams travel through the same core and mode, the illumination has inherently low
167 sensitivity to bending. In the collection path, since only intensity is collected though the

168 MCF cores, the detection is essentially insensitive to fiber bending. The inherently low
169 sensitivity to bending together with the high imaging speed enable imaging through
170 dynamically bent fibers, as we demonstrate in Supplementary Movie S2 and Fig. 5B.

171 **3D Imaging**

172 The low-coherence time gating of FiDHo allows axial sectioning of 3D targets [37].
173 To demonstrate this, we have performed several experiments whose results are presented in
174 Fig. 6. The experiments include imaging of a sample composed of two stacked USAF targets
175 with an axial separation of $300\mu\text{m}$ (Fig. 6A) and a thick chicken breast tissue (Fig. 6B). In
176 both experiments, the low-coherence gating together with the holographic reconstruction
177 allows axial-sectioning, depth measurement, and digitally refocused reconstruction of all
178 sample planes.

180 **Discussion**

181 We have demonstrated an approach for 3D lensless endoscopy that possess a unique
182 set of advantages, not jointly attainable with current approaches. These include video-rate
183 3D diffraction-limited, axially sectioned label-free imaging, in a calibration-free, bend-
184 insensitive system, without any moving distal elements. Importantly, all these advantages
185 are obtained in a simple system that employs commercially available MCFs, and with a
186 straightforward non-iterative computational reconstruction.

187 For optimal imaging performance the parameters of the MCF, distal-mirror, and
188 powers ratio of the object- and reference-arm should be set according to several
189 considerations. These considerations are analyzed in detail in section S2. To summarize, the
190 fiber diameter, D , dictates the FoV and maximal depth for diffraction-limited resolution
191 (Fig. 3), and should be as large as allowed by the selected application. The NA of the MCF
192 cores dictates the system resolution. Bend-sensitivity is minimized by choosing MCF cores
193 with low inter-core crosstalk, and single-mode propagation. The distal mirror distance, z_m ,
194 should be large enough such that the reference-wave phase is approximately constant over
195 each individual core, yielding: $z_m \gg \frac{Dd}{2\lambda}$, where d is the core diameter. Finally, the optimal
196 mirror reflectivity is dependent on the target reflectivity and is approximately 2% – 14%
197 for a reflected power fraction of 0.1% – 4% from the target.

198 A potential attractive application of FiDHo is for neuro-imaging, where a common
199 practice is to image the mouse brain through a cannula incorporating a glass coverslip [38].
200 The cover-slip can be naturally utilized as the partially reflecting mirror, without any
201 modifications to the distal probe.

202 The presented imaging results may be improved by angular-compounding using
203 multiple illuminations from different cores, at the expense of framerate. A larger FoV and
204 improved resolution may be obtained by extracting additional information from the power
205 distribution between the modes of each core [39, 40]. Using cameras with high framerates
206 and large well-depth will improve the signal to noise and imaging speed [41]. Finally, the
207 image reconstruction fidelity and resolution can be improved by employing compressed-
208 sensing reconstruction algorithms that incorporate prior knowledge on the target object
209 structure [42].

Experimental design

Fig. 1. depicts a simplified sketch of the experimental setup. The full experimental setup is presented in Fig. S1 and described below. The illumination is provided by a diode laser at a wavelength of $\lambda = 640\text{nm}$ and coherence length of $l_c \sim 400\mu\text{m}$ (iBeam-smart-640s, Toptica, $\sim 1\text{mW}$ at proximal facet). The illumination beam is split by a Mach-Zehnder Interferometer (MZI) using a polarizing beam splitter (PBS1, Thorlabs PBS251), and a non-polarizing 50-50 beam splitter (BS2, Thorlabs BS013). The powers ratio in the two arms is controlled by a half wave-plate (HWP1, Thorlabs WPH10M-633) placed before PBS1, and the polarizations are re-aligned by a second half-wave plate (HWP2, same as HWP1). The two arms need to be perfectly aligned, such that the two delayed beam replicas couple to the fundamental mode of a single MCF core. This is assured by using two separate 4-f telescopes (L1, L2, total of four $f = 100\text{mm}$ Thorlabs LA1509) placed in each of the MZI arms. Alternatively, the delayed replicas can be inherently aligned using a single-mode fiber (SMF) based MZI.

The two aligned beams exiting the MZI are coupled into a single core of the MCF using another telescope (L3, Thorlabs LB1901, $f = 75\text{mm}$ and L4, Thorlabs LA1979, $f = 200\text{mm}$) and a long working-distance objective (OBJ1, Mitutoyo 378-803-3, M Plan Apo 10x, 0.28 NA). A non-polarizing 50-50 beam-splitter (BS3, Thorlabs BP150) is placed between OBJ1 and the MCF proximal facet. The MCF proximal facet is imaged through BS3 onto a camera (sCMOS, Andor Zyla 4.2Plus) by another long working distance objective (OBJ2, same as OBJ1), a lens (L5, Thorlabs LA1979, $f = 200\text{mm}$) and a telescope with tunable magnification (ZOOM, Navitar 12X Zoom Lens System).

In order to minimize the proximal facet reflections in the camera image, two orthogonal linear polarizers (LP1, LP2: Thorlabs LPVISE100) are placed on the two ports of BS3 to effectively perform cross-polarized detection.

The reference arm length in the MZI is controlled by a two-mirror delay-line using a fine piezo-motor translator (Thorlabs PIA25 actuator and TIM101 controller) mounted on a larger translator (Thorlabs Z825B actuator and KDC101 controller) for phase-shifting and time gating, respectively.

At the distal end, the small partially reflecting mirror surface is placed at a distance of $z_m = 2\text{mm}$ from the fiber distal facet. The partial reflective mirror was fabricated by E-beam evaporation (EBPVD) of a 10nm -thick layer of Titanium on a 1mm glass slide. An additional 1mm -thick glass slide was used as a spacer, and an optical immersion oil with $n = 1.52$ refractive index was placed between the glass spacer and the fiber and mirror to reduce unwanted reflections. The targets were placed at different distances behind the partially reflecting mirror, either by holding the samples in air or with immersion oil or water between the mirror and the samples. An additional distal camera (CMOS, Allied Vision Mako U-130B) is used for acquiring the ground-truth images of the sample using a microscope objective (OBJ3, Olympus UPlanFL n, 10x 0.3 NA) and a lens (L6, Thorlabs LB1676, $f = 100\text{mm}$).

Suppression of spurious reflections

Since the system is designed to image weakly reflecting objects, it is very sensitive to unwanted and spurious reflections from the MCF proximal facet. The cross-polarized detection effectively reduces most of the proximal reflective background. Thanks to random birefringence of the MCF cores [43], the reflected signal from the object is randomly polarized after propagation through the MCF, and thus the cross-polarized detection only

259 halves the reflected object power on average. Spurious reflections at the MCF distal facet
 260 affect the single excited core, which is straightforward to spatially filter digitally.

261 Two additional sources of undesired reflections that are naturally present but do not
 262 appear in the simple form of eq.1 are the reflection of the reference beam from the object,
 263 and the reflection of the illumination beam from the distal mirror. The interference terms
 264 arising from these two unwanted reflections are effectively suppressed by low-coherence
 265 time gating, as we explain below. In general, the intensity pattern on the fiber distal facet is
 266 the result of interference of four reflected fields: two desired fields and two undesired fields.
 267 The two desired reflected fields are the reflection of the reference beam from the distal
 268 mirror, $E_{R,m}$, and the reflection of the object illumination beam from the object, $E_{I,o}$. The
 269 two undesired reflected waves are the reflection of the reference beam from the object, $E_{R,o}$,
 270 and the reflection of the object illumination beam from the distal mirror, $E_{I,m}$. Thus, the
 271 intensity pattern at the fiber distal (and proximal) facet is:

$$272 \quad I = |E_{R,o}e^{i\varphi_n} + E_{R,m}e^{i\varphi_n} + E_{I,o} + E_{I,m}|^2 \quad (3)$$

273 where φ_n is the phase-shifting phase.

274 The phase-shifting reconstructed hologram will be composed of 4 interference
 275 terms:

$$276 \quad \underbrace{E_{I,o}E_{R,m}^*}_A + \underbrace{E_{I,m}E_{R,m}^*}_B + \underbrace{E_{I,o}E_{R,o}^*}_C + \underbrace{E_{I,m}E_{R,o}^*}_D \quad (4)$$

277 The first term (A) is the desired signal, composed of the interference of the object
 278 illumination beam reflected from the object with the reference beam reflected from the
 279 mirror.

280 The three undesired terms (B-D) are as follows: The second term (B) arises from
 281 interference of the two reflections from the mirror and produces a large coherent
 282 background. The third term (C) results from two reflections from the object itself, and the
 283 last term (D) is the conjugate of (A) and will result in a defocused coherent background in
 284 the reconstruction. Without coherence-gating it would be very challenging to impossible to
 285 filter out the undesired interference terms. However, the four interferences occur at four
 286 distinct time delays between the reference arm and the object illumination arm, $\tau_A =$
 287 $\frac{2z_o}{c}$, $\tau_B = 0$, $\tau_C = 0$, $\tau_D = -\frac{2z_o}{c}$.

288 Using a source with a coherence length of $l_c \ll 2z_o$ allows to effectively suppress
 289 the unwanted interference terms by setting the time-delay between the two arms to $\tau = \tau_A$.
 290 A shorter coherence length source would be beneficial to both improve the axial-sectioning
 291 resolution and reduce the minimal working distance.

292 Digital filtering of MCF pixelation

293 Due to the low fill-factor of the MCF cores, the holographically reconstructed field
 294 is strongly pixelated at the fiber distal facet plane (Fig. 1 B, inset). This pixelation manifest
 295 itself as "ghosts" replicas in the images reconstructed by backpropagating the pixelated raw
 296 fields (Fig. S2 C), which are the result of the MCF under-sampling the fields. These are
 297 digitally filtered in a straightforward manner by applying a low-pass filter to the 2D Fourier
 298 transform of the reconstructed fields, i.e., by Fourier-interpolating the holographically
 299 measured fields, effectively interpolating the fields between the cores at the fiber facet (Fig.
 300 S2 D). We set the cutoff frequency of the low-pass filter to $k_{cutoff} = \pi/p$, where p is the
 301
 302
 303
 304

305 core-to-core pitch. The Fourier interpolation also effectively limits the detection NA to \sim
306 $\lambda/2p$, which dictates the reconstructed fields resolution.

307 The presented results were obtained using an MCF with identical cores arranged on
308 an ordered grid with very low crosstalk (Schott 153385). We obtained similar results using
309 an MCF with inhomogeneous cores arranged on an imperfectly ordered grid (Fujikura
310 FIGH-06-300S) (Fig. S4). In this case of imperfectly ordered grid, the spatial cutoff
311 frequency of the Fourier interpolation filter was set according to the average pixel pitch. A
312 discussion on the effects of the various fiber parameters is presented in the Supplementary
313 materials.
314

H2: Supplementary Materials

Section S1: Theoretical resolution and field-of-view analysis.

Section S2: Choice of optimal system parameters

Fig S1: Experimental setup

Fig S2: Fourier Interpolation on ordered MCF

Fig S3: Resolution and field-of-view characterization, detailed figure

Fig S4: Imaging using a disordered MCF

Movie S1: Imaging a moving USAF target at 50 FPS.

Movie S2: Imaging a moving USAF target while bending the MCF.

References

- [1] B. A. Flusberg, E. D. Cocker, W. Piyawattanametha, J. C. Jung, E. L. M. Cheung and M. J. Schnitzer, "Fiber-optic fluorescence imaging," *Nature methods*, vol. 2, p. 941–950, 2005.
- [2] G. Oh, E. Chung and S. H. Yun, "Optical fibers for high-resolution in vivo microendoscopic fluorescence imaging," *Optical Fiber Technology*, vol. 19, p. 760–771, 2013.
- [3] E. Papagiakoumou, F. Anselmi, A. Bègue, V. De Sars, J. Glückstad, E. Y. Isacoff and V. Emiliani, "Scanless two-photon excitation of channelrhodopsin-2," *Nature methods*, vol. 7, p. 848–854, 2010.
- [4] R. Barankov and J. Mertz, "High-throughput imaging of self-luminous objects through a single optical fibre," *Nature communications*, vol. 5, p. 1–6, 2014.
- [5] S. M. Kolenderska, O. Katz, M. Fink and S. Gigan, "Scanning-free imaging through a single fiber by random spatio-spectral encoding," *Opt. Lett.*, vol. 40, p. 534–537, 2 2015.
- [6] T. Xie, D. Mukai, S. Guo, M. Brenner and Z. Chen, "Fiber-optic-bundle-based optical coherence tomography," *Optics letters*, vol. 30, p. 1803–1805, 2005.
- [7] L. M. Wurster, L. Ginner, A. Kumar, M. Salas, A. Wartak and R. A. Leitgeb, "Endoscopic optical coherence tomography with a flexible fiber bundle," *Journal of Biomedical Optics*, vol. 23, p. 066001, 2018.
- [8] N. Bozinovic, C. Ventalon, T. Ford and J. Mertz, "Fluorescence endomicroscopy with structured illumination," *Optics express*, vol. 16, p. 8016–8025, 2008.
- [9] J. Mertz, "Optical sectioning microscopy with planar or structured illumination," *Nature methods*, vol. 8, p. 811, 2011.
- [10] Y. Choi, C. Yoon, M. Kim, T. D. Yang, C. Fang-Yen, R. R. Dasari, K. J. Lee and W. Choi, "Scanner-free and wide-field endoscopic imaging by using a single multimode optical fiber," *Physical review letters*, vol. 109, p. 203901, 2012.

- [11] A. Porat, E. R. Andresen, H. Rigneault, D. Oron, S. Gigan and O. Katz, "Widefield lensless imaging through a fiber bundle via speckle correlations," *Optics express*, vol. 24, p. 16835–16855, 2016.
- [12] N. Stasio, C. Moser and D. Psaltis, "Calibration-free imaging through a multicore fiber using speckle scanning microscopy," *Optics letters*, vol. 41, p. 3078–3081, 2016.
- [13] J. Shin, B. T. Bosworth and M. A. Foster, "Compressive fluorescence imaging using a multi-core fiber and spatially dependent scattering," *Optics letters*, vol. 42, p. 109–112, 2017.
- [14] J. Shin, D. N. Tran, J. R. Stroud, S. Chin, T. D. Tran and M. A. Foster, "A minimally invasive lens-free computational microendoscope," *Science advances*, vol. 5, p. eaaw5595, 2019.
- [15] I. T. Leite, S. Turtaev, D. E. B. Flaes and T. Čižmár, "Observing distant objects with a multimode fibre-based holographic endoscope," *arXiv preprint arXiv:2011.03600*, 2020.
- [16] N. Shekel and O. Katz, "Using fiber-bending-generated speckles for improved working distance and background rejection in lensless micro-endoscopy," *Optics Letters*, vol. 45, p. 4288–4291, 2020.
- [17] A. J. Thompson, C. Paterson, M. A. A. Neil, C. Dunsby and P. M. W. French, "Adaptive phase compensation for ultracompact laser scanning endomicroscopy," *Opt. Lett.*, vol. 36, p. 1707–1709, 5 2011.
- [18] S. Bianchi and R. Di Leonardo, "A multi-mode fiber probe for holographic micromanipulation and microscopy," *Lab Chip*, vol. 12, no. 3, pp. 635–639, 2012.
- [19] T. Čižmár and K. Dholakia, "Exploiting multimode waveguides for pure fibre-based imaging," *Nature communications*, vol. 3, p. 1–9, 2012.
- [20] E. R. Andresen, G. Bouwmans, S. Monneret and H. Rigneault, "Two-photon lensless endoscope," *Opt. Express*, vol. 21, p. 20713–20721, 9 2013.
- [21] I. N. Papadopoulos, S. Farahi, C. Moser and D. Psaltis, "High-resolution, lensless endoscope based on digital scanning through a multimode optical fiber," *Biomedical optics express*, vol. 4, p. 260–270, 2013.
- [22] S. C. Warren, Y. Kim, J. M. Stone, C. Mitchell, J. C. Knight, M. A. A. Neil, C. Paterson, P. M. W. French and C. Dunsby, "Adaptive multiphoton endomicroscopy through a dynamically deformed multicore optical fiber using proximal detection," *Opt. Express*, vol. 24, p. 21474–21484, 9 2016.

- [23] U. Weiss and O. Katz, "Two-photon lensless micro-endoscopy with in-situ wavefront correction," *Opt. Express*, vol. 26, p. 28808–28817, 10 2018.
- [24] S. Li, S. A. R. Horsley, T. Tyc, T. Cizmar and D. B. Phillips, "Guide-star assisted imaging through multimode optical fibres," *arXiv preprint arXiv:2005.06445*, 2020.
- [25] M. Plöschner, T. Tyc and T. Čižmár, "Seeing through chaos in multimode fibres," *Nature Photonics*, vol. 9, p. 529–535, 2015.
- [26] G. S. D. Gordon, M. Gataric, A. G. C. P. Ramos, R. Mouthaan, C. Williams, J. Yoon, T. D. Wilkinson and S. E. Bohndiek, "Characterizing Optical Fiber Transmission Matrices Using Metasurface Reflector Stacks for Lensless Imaging without Distal Access," *Phys. Rev. X*, vol. 9, no. 4, p. 041050, 12 2019.
- [27] W. Choi, M. Kang, J. H. Hong, O. Katz, Y. Choi and W. Choi, *Fourier holographic endoscopy for label-free imaging through a narrow and curved passage*, 2020.
- [28] V. Tsvirkun, S. Sivankutty, K. Baudelle, R. Habert, G. Bouwmans, O. Vanvincq, E. R. Andresen and H. Rigneault, "Flexible lensless endoscope with a conformationally invariant multi-core fiber," *Optica*, vol. 6, p. 1185–1189, 2019.
- [29] R. Kuschmierz, E. Scharf, N. Koukourakis and J. W. Czarske, "Self-calibration of lensless holographic endoscope using programmable guide stars," *Optics letters*, vol. 43, p. 2997–3000, 2018.
- [30] E. Scharf, R. Kuschmierz and J. Czarske, "Holographic lensless fiber endoscope with needle size using self-calibration," *tm-Technisches Messen*, vol. 86, p. 144–150, 2019.
- [31] E. Scharf, J. Dremel, R. Kuschmierz and J. Czarske, "Video-rate lensless endoscope with self-calibration using wavefront shaping," *Optics Letters*, vol. 45, p. 3629–3632, 2020.
- [32] O. Coquoz, R. Conde, F. Taleblou and C. Depeursinge, "Performances of endoscopic holography with a multicore optical fiber," *Applied optics*, vol. 34, p. 7186–7193, 1995.
- [33] A. T. Saucedo, F. M. Santoyo, M. De la Torre-Ibarra, G. Pedrini and W. Osten, "Endoscopic pulsed digital holography for 3D measurements," *Optics express*, vol. 14, p. 1468–1475, 2006.
- [34] M. R. Hughes, "Inline holographic microscopy through fiber imaging bundles," *Applied Optics*, vol. 60, p. A1–A7, 2020.
- [35] T. N. Ford, K. K. Chu and J. Mertz, "Phase-gradient microscopy in thick tissue with oblique back-illumination," *Nature Methods*, vol. 9, p. 1195–1197, 2012.

- [36] V. Emiliani, A. E. Cohen, K. Deisseroth and M. Häusser, "All-Optical Interrogation of Neural Circuits," *Journal of Neuroscience*, vol. 35, p. 13917–13926, 2015.
- [37] Z. Yaqoob, J. Wu, E. J. McDowell, X. Heng and C. Yang, "Methods and application areas of endoscopic optical coherence tomography," *Journal of biomedical optics*, vol. 11, p. 063001, 2006.
- [38] Y. Adam, J. J. Kim, S. Lou, Y. Zhao, M. E. Xie, D. Brinks, H. Wu, M. A. Mostajo-Radji, S. Kheifets, V. Parot and others, "Voltage imaging and optogenetics reveal behaviour-dependent changes in hippocampal dynamics," *Nature*, vol. 569, p. 413–417, 2019.
- [39] A. Orth, M. Ploschner, E. R. Wilson, I. S. Maksymov and B. C. Gibson, "Optical fiber bundles: Ultra-slim light field imaging probes," *Science advances*, vol. 5, p. eaav1555, 2019.
- [40] A. Orth, M. Ploschner, I. S. Maksymov and B. C. Gibson, "Extended depth of field imaging through multicore optical fibers," *Optics express*, vol. 26, p. 6407–6419, 2018.
- [41] A. Dubois, K. Grieve, G. Moneron, R. Lecaque, L. Vabre and C. Boccard, "Ultrahigh-resolution full-field optical coherence tomography," *Applied optics*, vol. 43, p. 2874–2883, 2004.
- [42] D. J. Brady, K. Choi, D. L. Marks, R. Horisaki and S. Lim, "Compressive Holography," *Opt. Express*, vol. 17, p. 13040–13049, 7 2009.
- [43] X. Chen, K. L. Reichenbach and C. Xu, "Experimental and theoretical analysis of core-to-core coupling on fiber bundle imaging," *Optics express*, vol. 16, p. 21598–21607, 2008.

327
328
329

330 **Acknowledgments**

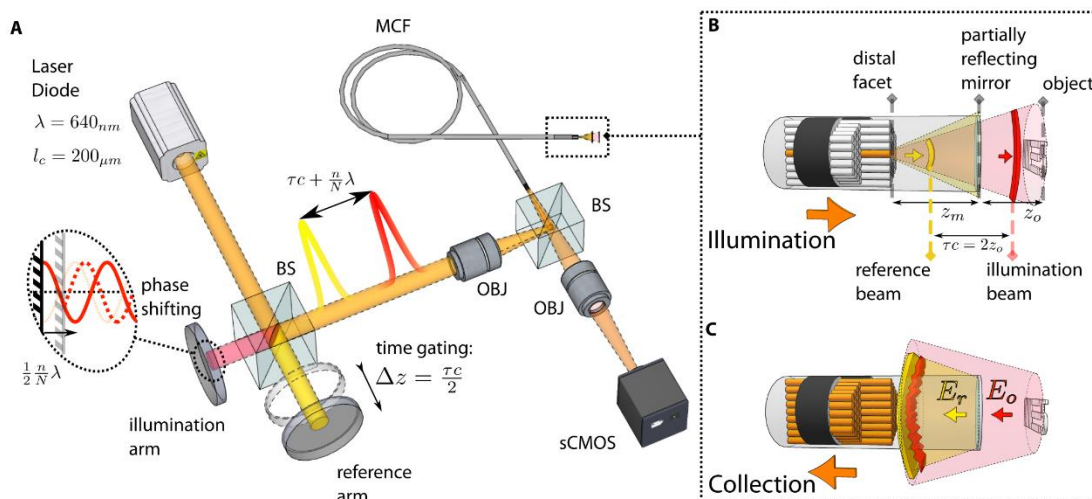
331
332 **General:** We thank the Hebrew University Center for Nanoscience and Nanotechnology for
333 distal mirror fabrication, and Tali Brooks for proofreading the manuscript.
334

335 **Funding:** This work received funding from the European Research Council (ERC) Horizon
336 2020 research and innovation program (grant no. 677909), Azrieli foundation, Israel
337 Science Foundation (1361/18), Israeli Ministry of Science and Technology (Grant
338 712845).
339

340 **Author contributions:** NB and OK conceived the idea and performed analytical analysis,
341 NB performed numerical simulations, experimental measurements, and data analysis. NB
342 and OK wrote the manuscript.
343

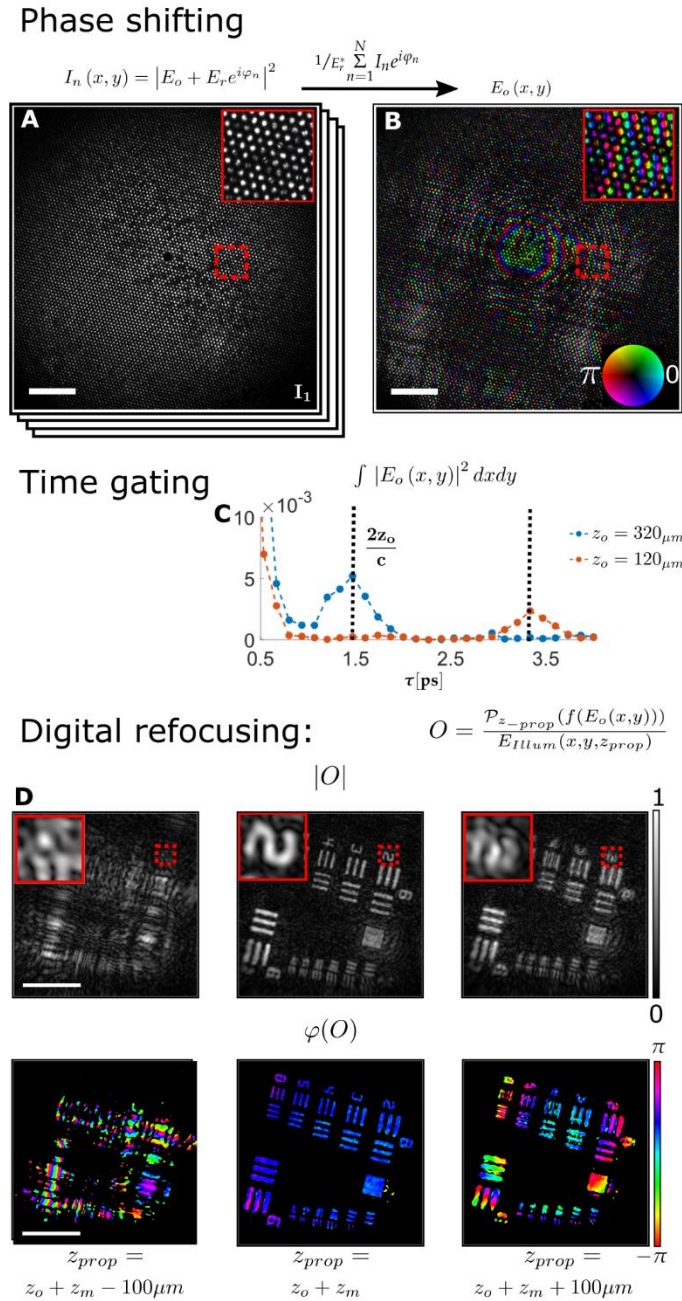
344 **Competing interests:** The authors declare no competing interests.
345

346 **Data and materials availability:** All data needed to evaluate the conclusions in the paper
347 are present in the paper and/or the Supplementary Materials.
348



352 **Fig. 1. Setup and principle of distal holographic endoscopy.** (A) A short coherence laser
 353 (orange) is split into two delayed replicas: an illumination beam and a reference
 354 beam (red and yellow, respectively) that are coupled into a single core of a multicore
 355 fiber (MCF). (B) At the distal MCF facet, the illumination beam and the reference
 356 beam are reflected from the target object and a partially reflecting distal mirror,
 357 respectively. (C) The intensity pattern of the interference between the reflected
 358 beams is relayed by the MCF to the proximal side, where it is imaged on a camera
 359 (A). Due to coherence gating, setting the relative time delay between the two arms
 360 to match the object-mirror distance, $\tau = 2Z_o/c$, results in measured interference
 361 only between the reflected illumination from the object and the reflected reference
 362 from the mirror. The object complex field is retrieved from N intensity-only
 363 proximal images, by phase-shifting the illumination arm (A, inset). See Fig. S1 for
 364 the full setup.
 365

Fig. 2



368
369
370
371
372
373
374
375
376
377
378

Fig. 2. Experimental holographic imaging of a resolution target. (A) N phase-shifted proximal intensity images $I_n(x, y)$ are used to retrieve the reflected object field on the distal facet, $E_o(x, y)$ (B). (C) Scanning the time delay between the reference and illumination arms reveals a peak of the total field energy at the correct target distance, as verified by placing a reflective target at two different distances (orange, blue); (D) Digital refocusing is achieved by back-propagating the measured distal field $E_o(x, y)$. The back-propagated field reveals the reflective USAF target in focus (top center) and with a flat phase (bottom center) at the correct distance ($z_{prop} = z_o + z_m$, $z_o = 340\mu m$), after normalizing by the illuminating field. At other propagation distances (left and right) the target is out-of-focus. (Insets, zoom-in on dashed rectangles). Scale bars: $100\mu m$

Fig. 3

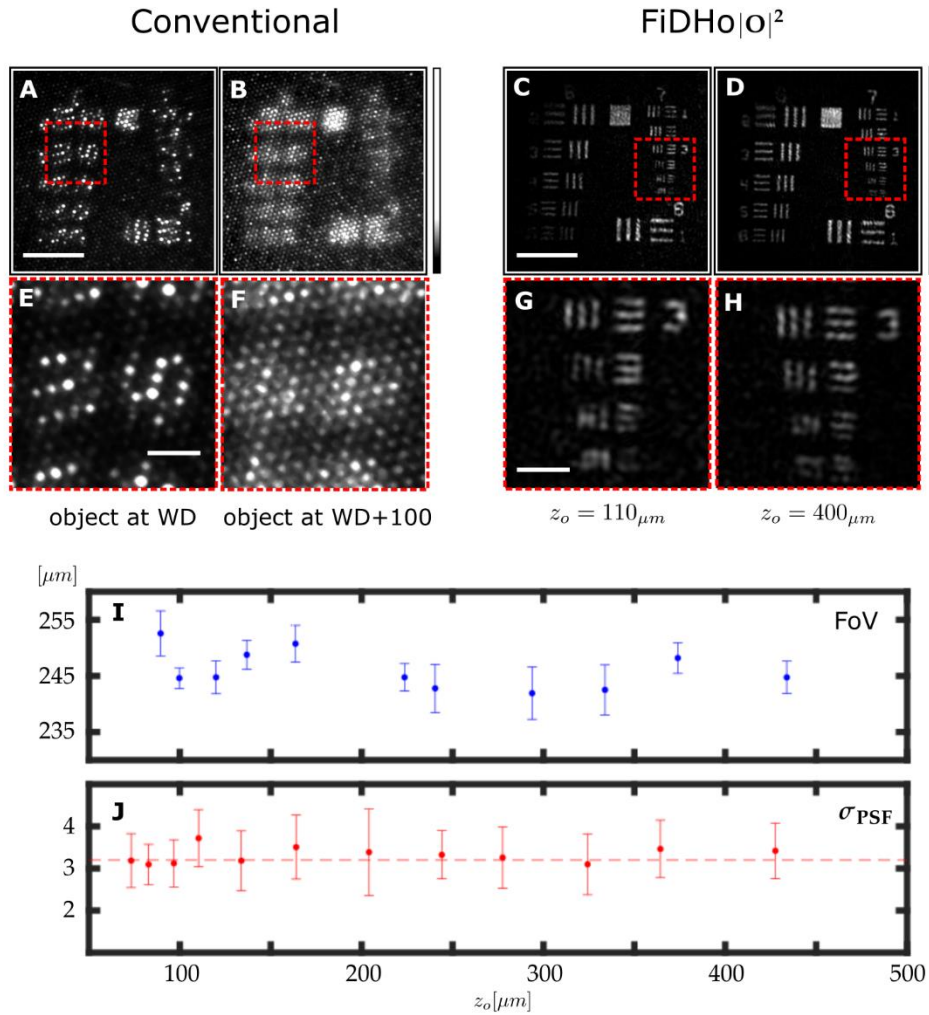


Fig. 3. Resolution and field-of-view characterization. Unlike conventional MCF-based microendoscopy, where each fiber core serves as one imaging pixel, the resolution is limited by the core-to-core pitch (A), and the object (a USAF 1951 target) is pixelated and in focus only at a specific working-distance (A, B). In FiDHo (C, D), the object is unpixelated and digitally focused on any distance, resolving features with a resolution that exceeds the fiber pixel pitch (E-H, zoom-in on dashed rectangles in A-D). (I) The system FoV, as measured by $1/e^2$ of the reconstructed intensity of a flat mirror (J) Imaging resolution as a function of depth, as retrieved from a knife-edge measurement (see section S1). Scale bars: (A-D) $100 \mu\text{m}$, (E-H) $25 \mu\text{m}$

380
381
382
383
384
385
386
387
388
389
390

Fig. 4

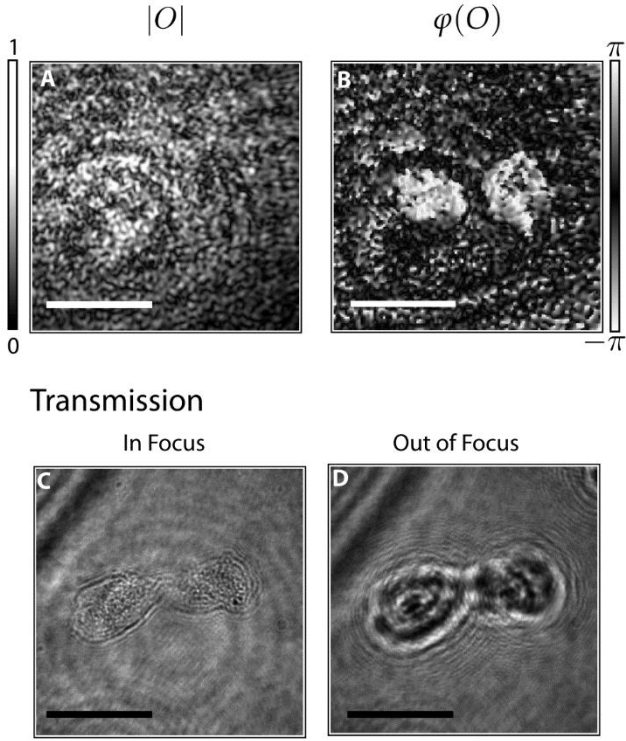
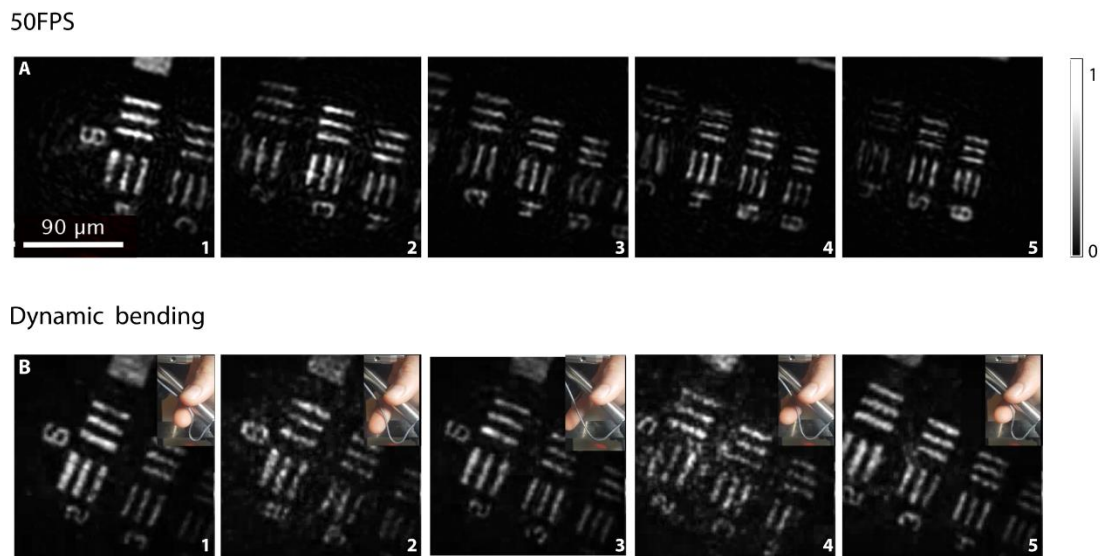


Fig. 4. Phase-contrast imaging (A, B) Reconstructed image of two cheek cells, placed in water on a microscope slide. The cells, which are not visible in the reconstructed field amplitude (A), are clearly visible in the reconstructed phase (B). (C, D) In-focus (C) and out-of-focus (D) widefield transmission microscope image of the cells. Scale bars- $80\mu m$

392
 393
 394
 395
 396
 397
 398

399 **Fig. 5**

400
401



402 **Fig. 5. Dynamic imaging at video-rate.** (A) Selected frames from a real-time video at 50
403 frames-per-second (FPS) of a moving resolution target (see Supplementary Movie
404 S1). (B) same as (A) when the fiber is dynamically bent, showing the insensitivity
405 to fiber orientation, and low sensitivity to bending (see Supplementary Movie S2)
406

402
403
404
405
406

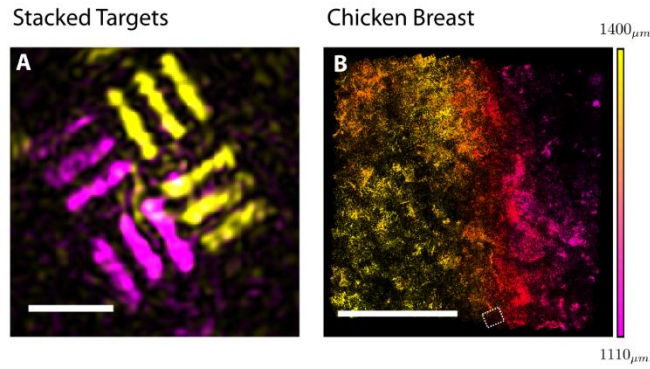
Fig. 6

Fig. 6. Imaging three-dimensional objects(A) A 3D image of a target composed of two stacked resolution targets with a spacing of $\sim 300\mu m$ reconstructed by super-posing two reconstructed images acquired with two appropriate time delays, $\tau = 2z_o/c$, with $z_o = 1030\mu m$ (pink) and $z_o = 1320\mu m$ (yellow). (B) An image of a chicken breast sample, reconstructed by stitching 11×11 sub-images, each with the fiber field of view (dashed rectangle). The varying depth of each sub-image is retrieved from the time-delay scan. Scale bars: A - $50\mu m$ B - $500\mu m$

408
409
410
411
412
413
414
415
416

Supplementary Files

This is a list of supplementary files associated with this preprint. Click to download.

- [FiDH0.natCom.SuppMat.pdf](#)
- [60FPSGroup6.avi](#)
- [5Submission0.mp4.mp4](#)